ELSEVIER

Chemical Engineering Science 60 (2005) 6085–6093

Chemical Engineering Science

www.elsevier.com/locate/ces

Calculation of flow fields in two and three-phase bubble columns considering mass transfer

D. Wiemann, D. Mewes*

Institute of Process Engineering, University of Hannover, Callinstrasse 36, 30167 Hannover, Germany

Received 2 December 2004; received in revised form 11 April 2005; accepted 11 April 2005
Available online 13 June 2005

Abstract

The dimension of bubble column reactors is often based on empirical correlations. Very popular is the axial dispersion model. However, the applicability of these models is limited to the experimental conditions for which the dispersion coefficients are measured, because backmixing depends strongly on the columns dimension and the flow regime. This paper presents a numerical method for the calculation of the three-dimensional flow fields in bubble columns based on a multi-fluid model. Therefore, the local bubble size distribution is considered by a transport equation for the mean bubble volume, which is obtained from the population balance equation. For comparison with experimental results, the axial dispersion coefficients in the liquid and gas phase are calculated from the instationary, three-dimensional concentration fields of a tracer. The model is then extended to include mass transfer between the gas and liquid phase. Increasing mass transfer rates significantly influence the flow pattern. For several applications, a dispersed solid phase is added. For the calculation of three-phase gas–liquid–solid flow, the solid phase is considered numerically by an additional Eulerian phase.

Keywords: Bubble columns; Dispersion; Mass transfer; Population balance; Suspension; Multiphase reactor

1. Introduction

The flow field in the stationary liquid phase of bubble column reactors is induced by the rising bubble swarm. In dependence of the superficial gas velocity, either the homogeneous or the heterogeneous flow regime arise. The homogeneous flow regime is present for low superficial gas velocities. The bubbles rise up straightforward and the interactions between the bubbles can be neglected. Therefore, the bubble diameter is not influenced by break-up and coalescence processes. With increasing superficial gas velocity, the local volume fraction of gas increases, thus, interactions between the bubbles become important. As a consequence, the increasing coalescence of bubbles leads to the formation of large bubbles. The resulting bubble size distribution is bimodal thus the gas phase can be divided into a small and large-bubble fraction. The liquid flow pattern is characterized by several large-scale vortices in the order of the column diameter. As a consequence, the vortical flow pattern and the coalescence and break-up of bubbles cause a residence time distribution in the liquid and the gas phase. For the dimension of bubble columns, these residence time distributions have to be considered since the overall mass transfer rate depends on them. Many experimental investigations of the mixing process in bubble columns have been performed, e.g. Mangartz and Pilhofer (1980) and Shetty et al. (1992) perform experimental investigations of backmixing in the gas phase within laboratory scale bubble columns. Backmixing in the liquid phase has been investigated by Ohki and Inoue (1970) and Degaleesan et al. (1996), for instance. Recently, Yang and Fan (2003) investigated backmixing of the liquid phase in pressurized bubble columns.

For the description of backmixing, several models have been developed as summarized by Levenspiel (1999) and Fogler (1999). One of the most popular ones for backmixing in bubble columns is the axial dispersion model, which

* Corresponding author. Tel.: +49 511 762 3828; fax: +49 511 762 3031.
E-mail addresses: wiemann@ifv.uni-hannover.de (D. Wiemann), dms@ifv.uni-hannover.de (D. Mewes).

0009-2509/$ - see front matter © 2005 Elsevier Ltd. All rights reserved.
doi:10.1016/j.ces.2005.04.054

describes the deviation from ideal plug flow. The mass flux due to dispersion is described in analogy to molecular transport, although both phenomena differ in their physical nature. The resulting molar flux density

$$\dot{n} = -(E + D)\frac{\partial c}{\partial x} \tag{1}$$

is described in dependence of the concentration gradient. In Eq. (1), the dispersion coefficient is labeled E and the molecular diffusion coefficient is D. In bubble columns, the molecular dispersion coefficient can be neglected with respect to the dispersion coefficient. Considering only axial dispersion the mass balance for a species A is written as

$$\frac{\partial c}{\partial t} + \frac{j_i}{\alpha_i}\frac{\partial c}{\partial x} = E_{i,\mathrm{ax}}\frac{\partial^2 c}{\partial x^2}, \quad i = g, l. \tag{2}$$

Therefore, a constant volume fraction of gas and a constant dispersion coefficient along the column height are assumed. In dependence of the kind of tracer injection, several solutions of Eq. (2) are published to determine the dispersion coefficient.

For a pulsewise tracer injection, a constant tracer concentration is reached in the column for long times provided the liquid is operated batchwise. The solution of Eq. (2) enables the calculation of the dispersion coefficient. From Ohki and Inoue (1970), an approximative solution is given for the pulsewise tracer injection considering a batch-operated liquid and the following initial and boundary conditions:

$$\frac{\partial c}{\partial x} = 0, \quad x = 0, L, \tag{3}$$

$$c(x, 0) = c_0 \quad \text{for } 0 \leqslant x \leqslant \delta, \tag{4}$$

$$c(x, 0) = 0 \quad \text{for } x \geqslant \delta. \tag{5}$$

In Eqs. (4) and (5), the height filled with tracer is labeled δ. Considering Eqs. (3)–(5), the solution of Eq. (2) is given by a series of infinitive terms

$$\frac{c(x,t)}{c_\infty} = 1 + 2\sum_{n=1}^{\infty}\left(\cos\left(\frac{n\pi}{H}x\right)\exp\left(-\left(\frac{n\pi}{H}\right)^2 E_{\mathrm{ax},l}t\right)\right). \tag{6}$$

In Eq. (6), the dispersion height is labeled H, the distance between the position of the tracer injection and the measuring point is x and the time after the tracer injection is t. The left-hand side of Eq. (6) is the ratio of the time-dependent tracer concentration to the constant tracer concentration for long times. For a given time-dependent tracer concentration field, the dispersion coefficient can be calculated using the method of least squares.

An alternative solution of Eq. (2) is given by Gray and Prados (1963). For the determination of the gas-phase dispersion, the tracer is continuously fed into the rising bubble swarm with a time-dependent sinusoidal concentration. Backmixing is then characterized by the change in the amplitude. For this approach, the bubble column is assumed to be represented by a linear response system. The experimental results from Mangartz and Pilhofer (1980) approve this assumption. Thus, the axial dispersion coefficient is calculated to

$$E_{\mathrm{ax},g} = \frac{j_g^3}{\alpha_g^3 \omega^2 H}\ln\left(\frac{c_{\mathrm{in}}}{c_{\mathrm{out}}}\right). \tag{7}$$

In Eq. (7), the angular frequency of the signal is ω, the dispersion height is H and the integrated gas volume fraction is α_g.

2. Modeling of bubbly flow

For the description of the three-dimensional, instationary flow-field, an Euler-multi-fluid model is used. This approach is numerically more efficient than the alternative Euler–Lagrange approach. For the multi-fluid approach, each phase is described by a quasi-continuous phase independent of its physical phase distribution. One of the key parameters for the design of bubble columns is the local interfacial area density since the momentum, energy and mass transfer rates are directly proportional to it. Therefore, Ishii and Kim (2004) propose a transport equation for the interfacial area.

Several numerical calculations of the flow fields in bubble columns have been published using the multi-fluid approach, e.g. by Sokolichin and Eigenberger (1999), Krishna et al. (1999) or Sanyal et al. (1999). However, only Lehr et al. (2002) consider the local bubble size distribution based on a population balance approach.

In this work, the multi-fluid model is coupled with a population balance equation approach according to Lehr et al. (2002). The interfacial area density is calculated with a transport equation for the mean bubble diameter considering bubble break-up and coalescence processes. For the heterogeneous flow regime one transport equation for each of the small and large bubble fraction is solved. Both transport equations are coupled by exchange terms due to bubble coalescence and break-up. The implementation of these transport equations into the CFD-code CFX-5.7 enables the calculation of the three-dimensional, time-dependent flow field in dependence of the local bubble size.

3. Conservation of momentum

For each phase one momentum balance equation is solved. This is written to

$$\frac{\partial}{\partial t}(\alpha_i \rho_i \vec{u}_i) + \nabla(\alpha_i(\rho_i \vec{u}_i \vec{u}_i)) = -\alpha_i \nabla p_i + \nabla(\alpha_i \eta_i(\nabla \vec{u}_i + (\nabla \vec{u}_i)^T)) + \vec{F}_{\mathrm{mass}} + \alpha_i \rho_i \vec{g} + \vec{F}_{ij}, \quad i = 1, 2, l. \tag{8}$$

The temporal and convective changes of momentum on the left-hand side of Eq. (8) are balanced by several forces on the right-hand side. These forces are due to the bulk pressure gradient, shear, secondary fluxes due to mass transfer, gravitational forces and interphase momentum transfer. For the multi-fluid approach, in particular, modeling of the interphase momentum transfer is important. The most important interphase force is due to interphase drag. In addition, other forces like transversal lift-force or added mass force are also present in bubbly flow. However, the modeling of these forces and their implementation into the multi-fluid approach are still discussed (Loth, 2000; Joshi, 2001; Sokolichin et al., 2004). For bubble columns with diameters larger than 15 cm, the added mass force can be neglected with respect to the drag force (Joshi, 2001). Therefore, in this work only the drag force is considered. The drag force per unit volume is

$$\vec{F}_{il} = C_D \frac{3}{4} \rho_l \frac{\alpha_i}{d_i} |\vec{u}_i - \vec{u}_l| (\vec{u}_i - \vec{u}_l) \quad i = 1, 2. \tag{9}$$

The drag coefficient is calculated according to Clift et al. hyperlinkbib3(1978),

$$C_D = \max \left[\frac{24}{Re}(1 + 0.1 Re^{0.75}); \min \left\{ \max \left(0.44, \frac{2}{3} Eo^{1/2} \right), \frac{8}{3} \right\} \right], \tag{10}$$

in dependence of the Reynolds and Eotvos number

$$Re_i = \frac{|\vec{u}_i - \vec{u}_l| d_i}{\nu_l} \tag{11}$$

$$Eo = \frac{g(\rho_l - \rho_i) d_i^2}{\sigma}. \tag{12}$$

In Eq. (12), the surface tension between the liquid and gas phase is σ. The Sauter bubble diameter d_i is calculated from a transport equation for the mean bubble volume. Due to bubble coalescence and break-up, second-order fluxes arise in the momentum equation for the small and large bubble fraction. These fluxes are considered in addition to the terms given in Eq. (1). In case of mass transfer, the term

$$\vec{F}_{\text{mass}} = \begin{cases} -\dot{M}_{i \to j} \vec{u}_i & \text{phase } i, \\ +\dot{M}_{i \to j} \vec{u}_i & \text{phase } j, \end{cases} \tag{13}$$

arises in the momentum equation considering second-order momentum fluxes due to mass transfer from phase i to phase j.

4. Conservation of mass

The bulk mass balance equation for each phase is

$$\frac{\partial(\alpha_i \rho_i)}{\partial t} + \nabla(\alpha_i \rho_i \vec{u}_i) = \begin{cases} -\dot{M}_{i \to l}, & i = 1, 2, \\ +\dot{M}_{j \to l}, & i = l, \quad j = 1, 2, \end{cases} \tag{14}$$

considering mass transfer from the gaseous to the liquid phase. In addition, source terms due to bubble coalescence and break-up as given by Lehr et al. (2002) are considered.

In case of multi-component flow with N species, $(N-1)$ species mass balance equations are solved in addition to Eq. (14). The gas phase consists of two components, which are identical in their properties. One of these components is used as tracer. The liquid phase consists of a background fluid, a tracer, and in case of mass transfer the transferring components. The species mass balance equation is

$$\frac{\partial(\alpha_i \zeta_{Ai} \rho_i)}{\partial t} + \nabla(\alpha_i \zeta_{Ai} \rho_i \vec{u}_i) - \nabla(D_{Ai} \nabla(\rho_i \zeta_{Ai})) = \begin{cases} -\zeta_{Ai} \dot{M}_{i \to l}, & i = 1, 2, \\ +\zeta_{Aj} \dot{M}_{j \to l}, & i = l, \quad j = 1, 2. \end{cases} \tag{15}$$

The terms on the right-hand side of Eq. (15) represent mass fluxes due to interphase mass transfer. Again, source and sink terms due to bubble coalescence and break-up are considered in addition to Eq. (8). For the calculation of the mass transfer rate, the phase equilibrium at the gas–liquid interface is described following Henry's law. The phase equilibrium is described with

$$\rho_{A,pl} = p_{A,g} \, \rho_l \Big/ \left(\frac{\mu_l}{\mu_g} H \right). \tag{16}$$

In Eq. (16), the molar mass of the liquid and gas phase are labeled μ_l and μ_g. The Henry constant is H. The mass transfer rate is calculated to

$$\dot{m}_{i,l} = \frac{c_l}{c_l - c_{A,l}} \beta_l (\rho_{A,pl} - \rho_{A,l}), \tag{17}$$

with the bulk molar concentration of the liquid phase c_l and the bulk molar concentration of the transferred component $c_{A,l}$. The mass transfer coefficient is calculated from a Sherwood number in dependence of the bubble volume. For small Reynolds numbers, the bubbles are spherical shaped, whereas with increasing Reynolds number turbulent motions at the surface become more and more important and the bubbles loose their shape. Therefore, for small Reynolds numbers below

$$Re_{\text{crit}} = 3.73 \left(\frac{\rho_l \sigma^3}{g \eta^4} \right)^{0.209}, \tag{18}$$

the Sherwood number is calculated according to Brauer (1979)

$$Sh = Sh_\infty [(1 + 0.433 Re^2)^{-1} + 0.0000423]^{-0.055} \tag{19}$$

with

$$Sh_\infty = 2 + \frac{0.651 (Re\, Sc)^{1.72}}{1 + (Re\, Sc)^{1.22}}. \tag{20}$$

For larger Reynolds numbers, the correlation

$$Sh = 2 + 0.015 Re^{0.89} Sc^{0.7} \tag{21}$$

is used instead of Eq. (19).

5. Turbulence in the liquid phase

In bubbly two-phase flow, the turbulent velocity fluctuations in the liquid phase are caused by the shear-induced turbulence as well as due to the presence of bubbles. Several experimental investigations deal with the influence of a dispersed phase on the continuous phase turbulence. In this work, a modified form of the k–ε turbulence model is used. The influence of bubbles on the liquid turbulence is described following the proposal of Lopez de Bertodano et al. (1994). Therefore, additional terms are calculated in dependence of the interphase drag. The resulting kinetic energy and dissipation rate are calculated to

$$k_{\mathrm{res}} = k_l + k_b = k_l + \tfrac{1}{4}\alpha_1|\vec{u}_1|^2 + \tfrac{1}{4}\alpha_2|\vec{u}_2|^2,$$

$$\varepsilon_{\mathrm{res}} = \varepsilon_l + \varepsilon_b = \varepsilon_l + \frac{\vec{F}_{d,1,l}}{\rho_l}|\vec{u}_1| + \frac{\vec{F}_{d,2,l}}{\rho_l}|\vec{u}_2|. \tag{22}$$

The second and third term on the right-hand side of Eq. (22) represent the bubble-induced dissipation rate and turbulent energy for the small and the large bubbles. The gas phases viscosity is described by the molecular viscosity of the gas.

6. Modeling the solid phase

For several applications, a solid phase is dispersed thus a three-phase gas–liquid–solid flow arises. For the multi-fluid model the solid phase is described by an Eulerian phase. The momentum balance equation for the solid phase is

$$\frac{\partial}{\partial t}(\alpha_s\rho_s\vec{u}_s) + \nabla(\alpha_s\rho_s\vec{u}_s\vec{u}_s) = -\alpha_s\nabla p - \nabla p_s + \nabla(\alpha_s\overline{\overline{\tau_s}}) - \vec{F}_d + \rho_s\vec{g}. \tag{23}$$

The first term on the right-hand side of Eq. (23) describes forces due to the bulk pressure gradient. The second term accounts for the additional solids pressures. Also, the third term considers forces from the motion of the particles. The last two terms consider interfacial momentum transfer and gravitational acceleration. For the calculation of the solids pressure and the solids stress tensor, the kinetic theory of granular flow is applied. Recently, Wylie et al. (2003) proposed an extension of the kinetic theory to liquid–solid flow for three limiting cases. The relative volume fraction of solids within the liquid–solid suspension is

$$\varepsilon_s = \frac{\alpha_s}{\alpha_s + \alpha_l}. \tag{24}$$

The solids pressure is calculated as

$$p_s = 2\rho_s g_0 \varepsilon_s^2(1+e)\Theta_s + \rho_s\Theta_s. \tag{25}$$

The coefficient of restitution is labeled e and the granular temperature of the solids is Θ_s.

According to Syamlal et al. (1993), the granular temperature is calculated to

$$\Theta_s = -K_1\varepsilon_s\mathrm{tr}(\overline{\overline{D_s}}) + [K_1^2\mathrm{tr}^2(\overline{\overline{D_s}})\varepsilon_s^2 + 4K_4\varepsilon_s(K_2\mathrm{tr}^2(\overline{\overline{D_s}}) + 2K_3\mathrm{tr}(\overline{\overline{D}}^2))]^{0.5} \times (2\varepsilon_s K_4)^{-2}, \tag{26}$$

including the factors

$$K_1 = 2(1+e)\rho_s g, \tag{27}$$

$$K_2 = 4d_s\rho_s(1+e)\frac{\varepsilon_s g_0}{3\pi^{1/2}} - \frac{2}{3}K_3, \tag{28}$$

$$K_3 = \frac{d_s\rho_s}{2}\left(\frac{\pi^{1/2}}{3(3-e)}[1 + 0.4(1+e)(3e-1)\varepsilon_s g_0] + \frac{8\varepsilon_s g_0(1+e)}{5\pi^{1/2}}\right), \tag{29}$$

$$K_4 = \frac{12(1-e)^2\rho_s g_0}{d_s\pi^{1/2}}. \tag{30}$$

In Eq. (26), the tensor of deformation is defined as

$$\overline{\overline{D_s}} = \tfrac{1}{2}(\nabla u_s + (\nabla u_s)^{\mathrm{T}}). \tag{31}$$

The radial distribution function is calculated according to Lun and Savage (1986) to

$$g_0 = \left(1 - \frac{\varepsilon_s}{\varepsilon_{s,\max}}\right)^{-2.5/\varepsilon_{s,\max}} \tag{32}$$

with the maximum volume fraction of solids $\varepsilon_{s,\max}$. The solids stress tensor is calculated as

$$\overline{\overline{\tau_s}} = 2\mu_s\overline{\overline{D}}_s + \left(\lambda_s - \frac{2}{3}\mu_s\right)\mathrm{tr}(\overline{\overline{D_s}})\,\overline{\overline{I}}, \tag{33}$$

with the solids bulk viscosity according to Lun et al. (1984)

$$\lambda_s = \frac{4}{3}\varepsilon_s^2\rho_s d_s g_0(1+e)\left(\frac{\Theta_s}{\pi}\right)^{1/2} \tag{34}$$

and the solids shear viscosity

$$\mu_s = K_2\varepsilon_s\Theta_s^{1/2}. \tag{35}$$

The momentum transfer due to drag

$$\vec{F}_{sl} = C_D\frac{3}{4}\rho_l\frac{\alpha_s}{d_i}|\vec{u}_s - \vec{u}_l|\,(\vec{u}_s - \vec{u}_l) \tag{36}$$

between the liquid and the solid phase is calculated in dependence of the drag coefficient according to Wen and Yu (1966):

$$C_D = \varepsilon_l^{-1.65}\max\left(\frac{24}{Re'}(1 + 0.15Re'^{0.687}), 0.44\right). \tag{37}$$

The modified Reynolds number in Eq. (37) is calculated to

$$Re' = \varepsilon_l\frac{|u_s - u_l|d_p}{\nu_l}, \tag{38}$$

where ε_1 denotes the relative liquid volume fraction within the liquid–solid suspension. The solid particles also influence the turbulence in the liquid phase. For particles, which are small compared to the eddy length scale, turbulent fluctuations are damped, whereas large particles tend to attenuate the turbulent velocity fluctuations. In the present work, the influence of the solids on the liquid phase turbulence is not considered.

The mass transfer in three-phase flow can be influenced by the presence of dispersed solid particles, thus related to two-phase flow higher or lower mass transfer rates are present. In a review of mass transfer in gas–solid–liquid flow, Beenackers and van Swaaij (1993) emphasize that for low solids loadings of small but heavy particles, which are typical in slurry columns, only small changes with respect to two-phase flow have to be expected. Since a detailed model for the prediction of the liquid side mass transfer is not available and a closed theoretical understanding for the influence of suspended solids on the mass transfer rate is still missing, the mass transfer coefficient is calculated using Eqs. (19)–(21). This approach guarantees a conservative estimation for the liquid side mass transfer coefficient.

7. Numerical solution

The flow domain is discretized using a block-structured grid with hexahedral volumes. The edge length of the grid is 1 cm. Near the wall region, a finer grid is used. Since the instationary flow-fields are calculated, time steps in the range of 0.01–0.05 s are made. The convective terms are discretized with second-order accuracy. At the bottom of the column, the inlet boundary conditions are specified for the phase velocity, volume fraction and remaining properties. At the top of the column, the free surface is approximated by a boundary condition, which enables the gas phase to go out, whereas for the solid and liquid phase a free slip condition is applied, which permits them from passing through. In addition, below the top surface an outflow for liquid and solid is assumed in the circumferential direction.

8. Results

In the first part of the work, backmixing in the liquid and gaseous phase is determined. Therefore, a perfect tracer is added into the liquid and the gas phase. For the liquid phase, the tracer is injected pulsewise at the top of the column, whereas for the gaseous phase a continuous tracer injection is chosen. In an earlier work, the models ability to predict the interfacial area density and the bubble size have been already shown in detail by Lehr et al. (2002).

In Fig. 1, the time-dependent flow field of the liquid phase is shown for a column with 2 m height and 20 cm diameter. The liquid is operated batchwise, whereas the superficial gas velocity is 0.02 m/s. The streamlines of the liquid are coloured with the axial liquid velocity. The time interval between the instantaneous flow fields is 2 s.

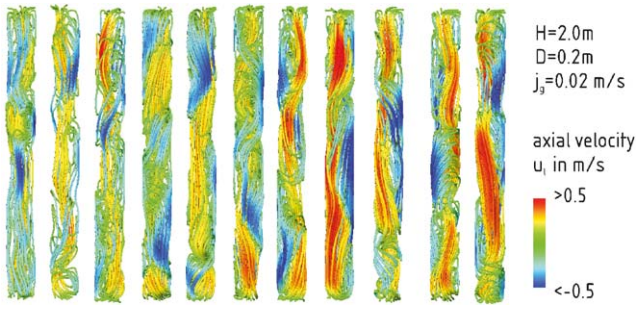

Fig. 1. Time-dependent flow field of the liquid phase.

Fig. 2. Dispersion of the liquid tracer.

The liquid phase is transported upwards in particular in the center region of the column. Near the column wall, the liquid flows downwards. The flow pattern is characterized by several large-scale vortices, which move in the axial and circumferential direction. For the same time steps, the dispersion of the liquid tracer is shown in Fig. 2.

The tracer is first transported downwards near the column wall in accordance with the liquid flow field. With increasing time, the tracer is distributed over the whole cross-section of the column. For longer times, an almost homogeneous distribution of the tracer is obtained. For a laboratory scale bubble column, the liquid and gas phase dispersion are determined simultaneously. First, the liquid phase dispersion is discussed. For several points in the column, the time-dependent tracer concentration is calculated. These response curves are used to calculate the axial-dispersion coefficient according to Eq. (6). For the dimensionless representation, the Bodenstein number

$$Bo = \frac{j_g D}{E_{\mathrm{ax},l}} \tag{39}$$

and the Froude number

$$Fr = \frac{j_g^2}{gD} \tag{40}$$

are used. In Eqs. (39) and (40), the column diameter is labeled D. The calculated dispersion coefficients are shown

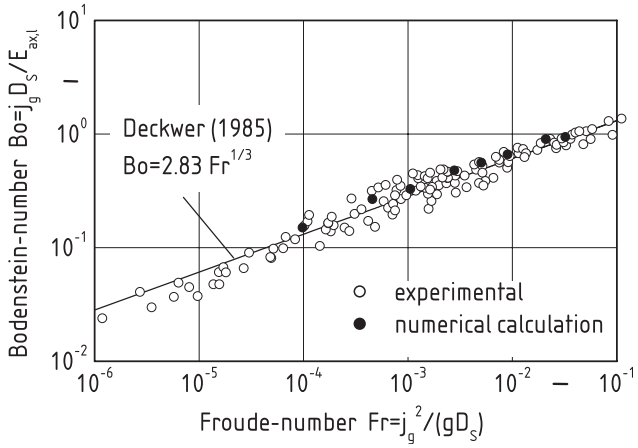

Fig. 3. Axial dispersion coefficient in dependence of superficial velocity.

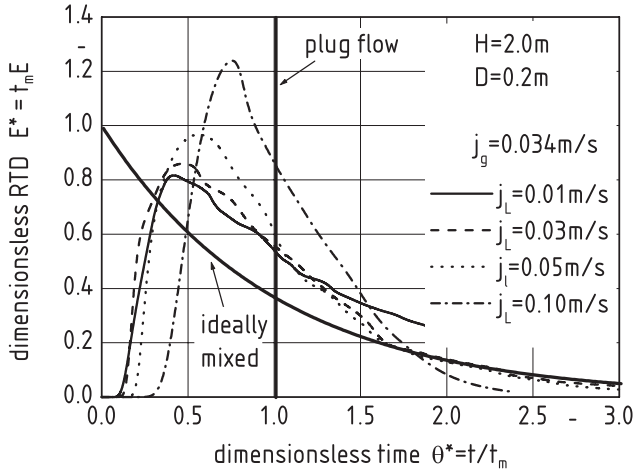

Fig. 4. Influence of superficial liquid velocity on liquid phase residence time distribution.

in Fig. 3. In addition to the calculated results, the experimental results are shown as reported by Deckwer (1992).

The calculated axial dispersion coefficients increase with increasing superficial gas velocity. This is in good agreement with the experimental results for which the dispersion coefficient increases to the power of one third with the superficial liquid velocity.

For several applications, a superficial liquid velocity is applied. To determine backmixing in these cases, the tracer is injected pulsewise at the liquid inlet. The time-dependent tracer concentration is then regarded at the top of the column. For the characterization of the mixing process, the mean residence time is defined as

$$t_m = \frac{\int_0^\infty t c(t)\mathrm{d}t}{\int_0^\infty c(t)\mathrm{d}t}. \tag{41}$$

The residence time distribution is defined as

$$E(t) = \frac{c(t)}{\int_0^\infty c(t)\mathrm{d}t}. \tag{42}$$

A dimensionless representation is obtained with

$$\theta = \frac{t}{t_m} \tag{43}$$

and

$$E^* = E(t)t_m. \tag{44}$$

The dimensionless residence time distribution is shown in dependence of the dimensionless time in Fig. 4. In addition to the calculated results, the limiting cases for an ideally stirred reactor and a plug flow reactor are given.

With increasing superficial liquid velocity, the dimensionless residence time distribution for the bubble column increases at larger values for the dimensionless time. After a maximum value is reached a decrease occurs. The higher the superficial liquid velocity, the higher the maximum value. For all cases the bubble column is operated between the limiting cases of an ideally stirred reactor and a plug flow reactor. With increasing superficial liquid velocity, the residence time distribution of a bubble column is shifted towards that of a plug flow reactor.

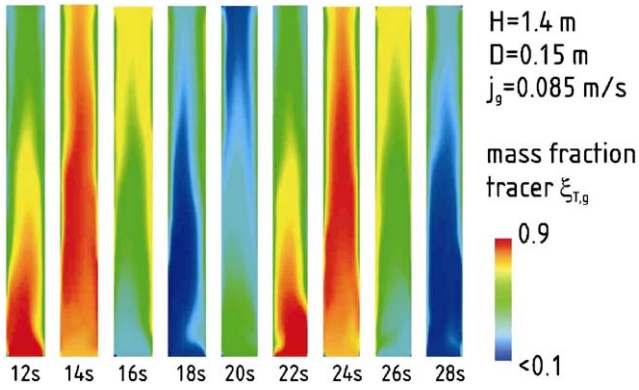

Fig. 5. Amplitude of the gas tracer.

For the gas phase, a sinusoidal tracer concentration is injected into the rising bubble swarm. The vortical flow structure, differences in the rising velocities and the coalescence and break-up of bubbles cause a residence time distribution. In Fig. 5, the calculated sinusoidal tracer signal is shown along the column height.

With increasing column height, only the amplitude of the signal is changed, whereas the frequency remains constant. This change in the amplitude is used to calculate the axial dispersion coefficient in the gas phase according to Eq. (7). The calculated axial dispersion coefficients for the gas phase are shown in Fig. 6.

For low superficial gas velocities corresponding to the homogeneous flow regime the dispersion coefficient increases slightly with the superficial gas velocity. For larger superficial gas velocities corresponding to the heterogeneous flow regime, the dispersion coefficient increases significantly with the superficial gas velocity. This is in accordance with the formation of a bi-modal bubble size distribution. The

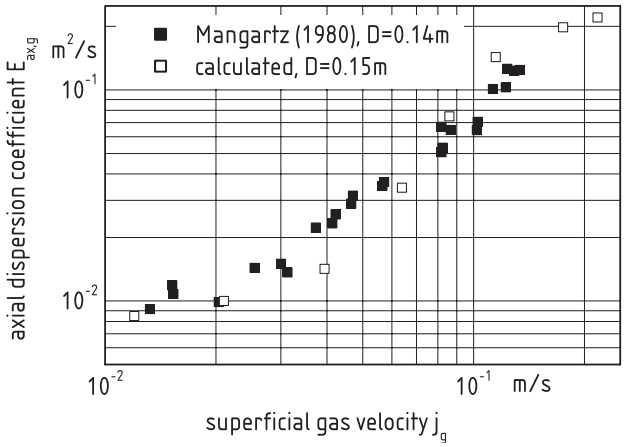

Fig. 6. Calculated dispersion coefficients for the gas phase.

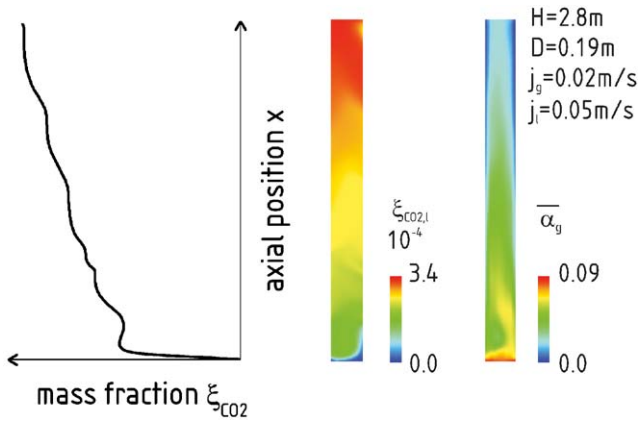

Fig. 8. Absorption of carbon dioxide into water.

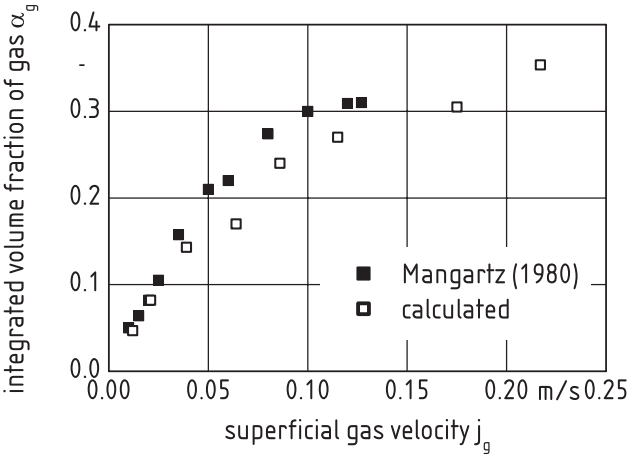

Fig. 7. Integrated volume fraction of gas.

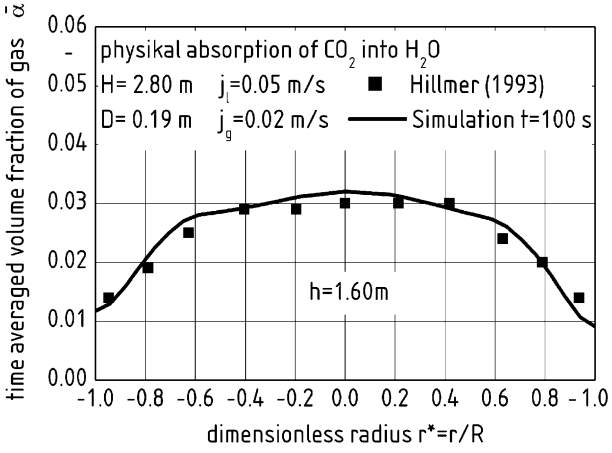

Fig. 9. Time-averaged volume fraction of gas.

large bubbles rise up faster than the smaller ones, thus a large amount of gas is transported in these bubbles. In addition, increasing coalescence and break-up of bubbles enhance the mixing process within the gas phase. Since not only the dispersion coefficient but also the volume fraction of gas is important for the design of bubble columns, the calculated integrated volume fraction of gas and experimental results are shown in Fig. 7. For large superficial velocities of the gas phase, the enhanced coalescence of bubbles leads to the formation of large bubbles, which rise up faster than the smaller ones. Therefore, in the heterogeneous flow regime a lowered increase in the overall gas volume fraction arises.

Based on the reasonable prediction of the hydrodynamic parameters the multi-fluid model is extended to include the absorption of the gas phase. Therefore, the physical absorption of carbon dioxide into water is considered. The absorption is calculated within a column of 2.8 m height and 19 cm diameter. The superficial velocity is 2 cm/s for the gas phase and 5 cm/s for the liquid phase. In Fig. 8, the instantaneous liquid phase mass fraction of carbon dioxide and the time-averaged volume fraction of gas are shown. The initial mass fraction in the liquid is zero. Due to the absorption process, the mass fraction of carbon dioxide within the liquid increases along the column height. The strong increase at the bottom and the scattering are caused due to backmixing in the liquid.

In accordance with the absorption process, the volume fraction of gas is reduced along the column height. The time-averaged volume fraction of gas decreases significantly with the column height. The radial profile of the time averaged gas volume fraction is shown in Fig. 9, for a cross section in height of 1.6 m. In addition the experimental results of Hillmer (1993) are given. The volume fraction is axisymmetric with the maximum at the column axis.

The absorption of the gas phase also reduces the overall momentum transfer to the liquid phase. Therefore, changes in the flow pattern have to be expected. In Fig. 10, the case of a fast chemical reaction is compared with the flow pattern for an inert flow.

Due to the absorption the volume fraction of gas is significantly reduced along the column height. The strong reduction of the gas volume fraction lowers the momentum

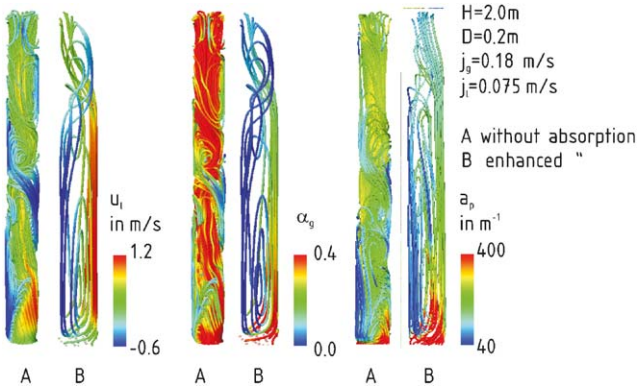

Fig. 10. Flow field with and without mass transfer.

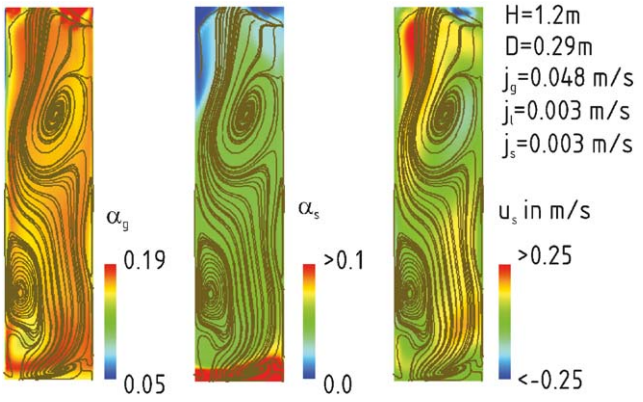

Fig. 11. Three-phase flow in a bubble column.

transfer to the liquid phase thus the flow structure is changed. In the case of inert flow, the flow field is characterized by several large-scale vortices, whereas for the chemical absorption the liquid circulates within one large loop. In accordance with the changes in the flow pattern and the volume fraction, the local interfacial area density is reduced.

For three-phase gas–liquid–solid flow a dispersed solid phase is added. The spherical particles are of 137 μm diameter and 2300 kg/m^3 density. The solid phase is considered in the model equations by its pressure and stress, which are calculated according to Eqs. (23)–(38). In Fig. 11, the instantaneous flow field within the three-phase column is shown. The liquid–solid suspension enters the column with a superficial velocity of 3 mm/s. The superficial gas velocity is set to 4.8 cm/s.

In addition to the volume fraction and the axial liquid velocity, the streamlines of the liquid are given as a texture. The vortical flow structure is similar to that of two-phase gas–liquid flow. The liquid is transported upwards in the central region of the column and downwards near the walls. For the given superficial velocities, full fluidization is not achieved. Thus, the volume fraction of solids decreases with the column height.

9. Conclusion

The three-dimensional, instationary flow fields in cylindrical bubble columns are calculated using a multi-fluid model coupled with a transport equation for the mean bubble diameter. Backmixing in the liquid and gaseous phase is calculated based on the dispersion of a perfect tracer. For comparison with experimental results, the axial dispersion coefficients are calculated. The predicted dispersion coefficients are in good agreement with experimental results. The absorption of the gas phase reduces the momentum transfer to the liquid phase thus the flow pattern is changed along the column height.

For three-phase flow, a dispersed solid phase is considered by an Eulerian phase. The solids pressure and viscosity are calculated using the theory of granular flow. The calculated flow pattern is similar to that of two-phase gas–liquid flow.

Notation

a	interfacial area density, m^{-1}
c	molar concentration, mol m^{-3}
C_D	drag coefficient
d	bubble diameter, m
D	column diameter, m
e	coefficient of restitution, dimensionless
E	dispersion coefficient, m^2 s^{-1}
F	force per volume, kg m^{-2} s^{-2}
g	gravitational acceleration, ms^{-2}
H	Henry coefficient, kg m^{-1} s^{-2}
j	superficial velocity, m s^{-1}
k	turbulent kinetic energy, m^2 s^{-2}
$\dot{m}$	mass flux density, kg m^{-2} s^{-1}
$\dot{n}$	molar flux density, mol m^{-2} s^{-1}
p	pressure, kg m^{-1} s^{-2}
t	time, s
u	velocity, m s^{-1}
x	coordinate, m

Greek letters

α	volume fraction
β	mass transfer coefficient, m s^{-1}
ε	turbulent kinetic energy dissipation rate, m^2 s^{-3}
η	dynamic viscosity, kg m^{-1} s^{-1}
μ	molecular weight, kg kmol^{-1}
ν	kinematic viscosity, m^2 s^{-1}
ξ	mass fraction
ρ	density, kg m^{-3}
σ	surface tension, kg s^{-2}

Subscripts

l	liquid
1	small bubble fraction
2	large bubble fraction

Acknowledgements

The authors gratefully acknowledge the financial support of the German Research Foundation (DFG). The computations are performed using the North German Supercomputing Combine (HLRN) in Hannover and Berlin.

References

Beenackers, A.A.C.M., van Swaaij, W.P.M., 1993. Mass transfer in gas–liquid slurry reactors. Chemical Engineering Science 48, 3109–3139.

Brauer, H., 1979. Particle/fluid transport processes. Progress in Chemical Engineering 17, 61–99.

Clift, R., Grace, J.R., Weber, M.E., 1978. Bubbles, Drops and Particles. Academic Press, New York, San Francisco, London.

Deckwer, W.-D., 1992. Bubble Column Reactors. Wiley, New York.

Degaleesan, S., Roy, S., Kumar, S.B., Dudukovic, M.P., 1996. Liquid mixing based on convection and turbulent dispersion in bubble columns. Chemical Engineering Science 51, 1967–1976.

Fogler, H.S., 1999. Elements of Chemical Reaction Engineering. third ed. Prentice-Hall, Englewood Cliffs, NJ.

Gray, R.I., Prados, J.W., 1963. Dynamics of packed gas absorber by frequency response analysis. A.I.Ch.E. Journal 9, 211–216.

Hillmer, G., 1993. Experimentelle Untersuchung und fluiddynamische Modellierung von Suspensionsblasensäulen. Ph.D. Thesis, University Erlangen-Nürnberg.

Ishii, M., Kim, S., 2004. Development of one-group interfacial area transport equation. Nuclear Science and Engineering 3, 257–273.

Joshi, J.B., 2001. Computational flow modeling and design of bubble column reactors. Chemical Engineering Science 21–22, 5893–5933.

Krishna, R., Urseanu, M.I., van Baten, J.M., Ellenberger, J., 1999. Influence of scale on the hydrodynamics of bubble columns operating in the churn-turbulent regime: experiments vs. Eulerian simulations. Chemical Engineering Science 21, 4903–4911.

Lehr, F., Millies, M., Mewes, D., 2002. Bubble-size distributions and flow fields in bubble columns. A.I.Ch.E. Journal 11, 2426–2443.

Levenspiel, O., 1999. Chemical Reaction Engineering. third ed. Wiley, New York.

Lopez de Bertodano, M., Lahey, R.T., Jones, O.C., 1994. Development of a k–ε model for bubbly two-phase flow. Journal of Fluids Engineering 1, 128–134.

Loth, E., 2000. Numerical approaches for motion of dispersed particles, droplets and bubbles. Progress in Energy and Combustion Science 3, 161–223.

Lun, C.K.K., Savage, F.B., 1986. The effects of impact velocity dependent coefficient of restitution on stress developed by sheared granular materials. Acta Mechanica 63, 15–44.

Lun, C.K.K., Savage, F.B., Jeffrey, D.J., Chepurniy, N., 1984. Kinetic theories for granular flow: inelastic particles in Couette flow and slightly inelastic particles in a general flow field. Journal of Fluid Mechanics 140, 223–256.

Mangartz, K.H., Pilhofer, T., 1980. Untersuchungen zur Gasphasen-dispersion in Blasensäulenreaktoren. Verfahrenstechnik 1, 40–44.

Ohki, Y., Inoue, H., 1970. Longitudinal mixing of the liquid phase in bubble columns. Chemical Engineering Science 1, 1–16.

Sanyal, J., Vasquez, S., Roy, S., Dudukovic, M.P., 1999. Numerical simulation of gas–liquid dynamics in cylindrical bubble column reactors. Chemical Engineering Science 21, 5071–5083.

Shetty, S.A., Kantak, M.V., Kelkar, B.G., 1992. Gas-phase backmixing in bubble column reactors. A.I.Ch.E. Journal 7, 1013–1026.

Sokolichin, A., Eigenberger, G., 1999. Applicability of the standard k–e turbulence model to the dynamic simulation of bubble columns: part I. Detailed numerical simulations. Chemical Engineering Science 13–14, 2273–2284.

Sokolichin, A., Eigenberger, G., Lapin, A., 2004. Simulation of buoyancy driven bubbly flow: established simplifications and open questions. A.I.Ch.E. Journal 1, 24–45.

Syamlal, M., Rogers, W., O'Brien, T.J., 1993. Technical Note DOE/METC-94/1004, Morgantown Energy Technology Center, Morgantown.

Wen, C.Y., Yu, Y.H., 1966. Mechanics of fluidization. Chemical Engineering Progress Symposium Series, vol. 62, p. 100.

Wylie, J.J., Koch, D.L., Ladd, A.J.C., 2003. Rheology of suspensions with high particle inertia and moderate fluid inertia. Journal of Fluid Mechanics 480, 95–118.

Yang, G.Q., Fan, L.-S., 2003. Axial liquid mixing in high-pressure bubble columns. A.I.Ch.E. Journal 8, 1995–2008.